

# Continuous-wave room-temperature diamond maser

Jonathan D. Breeze<sup>1,2</sup>, Enrico Salvadori<sup>3,4,5</sup>, Juna Sathian<sup>1</sup>, Neil McN. Alford<sup>1,2</sup> & Christopher W. M. Kay<sup>3,4,6</sup>

**The maser—the microwave progenitor of the optical laser—has been confined to relative obscurity owing to its reliance on cryogenic refrigeration and high-vacuum systems. Despite this, it has found application in deep-space communications and radio astronomy owing to its unparalleled performance as a low-noise amplifier and oscillator. The recent demonstration of a room-temperature solid-state maser that utilizes polarized electron populations within the triplet states of photo-excited pentacene molecules in a *p*-terphenyl host<sup>1–3</sup> paves the way for a new class of maser. However, *p*-terphenyl has poor thermal and mechanical properties, and the decay rates of the triplet sublevel of pentacene mean that only pulsed maser operation has been observed in this system. Alternative materials are therefore required to achieve continuous emission: inorganic materials that contain spin defects, such as diamond<sup>4–6</sup> and silicon carbide<sup>7</sup>, have been proposed. Here we report a continuous-wave room-temperature maser oscillator using optically pumped nitrogen–vacancy defect centres in diamond. This demonstration highlights the potential of room-temperature solid-state masers for use in a new generation of microwave devices that could find application in medicine, security, sensing and quantum technologies.**

Solid-state masers, developed in the 1960s, were realized by pumping the spin states of paramagnetic impurities, such as Cr<sup>3+</sup> ions doped into single-crystal sapphire (ruby). Pumping three-level systems with microwaves generates a population inversion—the requisite feature for amplification by stimulated emission in both masers and lasers—whereby a higher-energy state is more populated than a lower-energy state. For these early paramagnetic systems, cryogenic cooling was necessary to reduce the effects of spin–lattice relaxation, prolonging the lifetime of the population inversion and making continuous maser emission feasible.

The first demonstration of a room-temperature solid-state maser required more than 200 W of optical power to overcome the masing threshold, and produced a burst of microwave power at 1.45 GHz (ref. 1). This maser was subsequently improved and miniaturized using strontium titanate as the dielectric resonator material<sup>2,3</sup>, which lowered the optical pump threshold and volume by two orders of magnitude. However, the threshold pump rate per molecule remained the same at about 10<sup>4</sup> s<sup>−1</sup>. Even if continuous-wave operation could be achieved in organic triplet-based masers, heating is a problem because most of the absorbed optical pump power is dissipated through non-radiative relaxation processes and the organic hosts have poor thermal properties. For example, the pentacene host *p*-terphenyl has a low thermal conductivity of 0.1 W m<sup>−1</sup> K<sup>−1</sup> and a melting point of 230 °C.

Inorganic materials have better thermal and mechanical properties than do organic materials. Specifically, those that host spin defects offer a potential route to realizing continuous-wave room-temperature solid-state masers if the population of defect spin states can be polarized (inverted). Silicon carbide (SiC) is a promising candidate because its various types of spin defect can be addressed individually by tuning the wavelength of optical excitation and applying a magnetic field, which,

through the Zeeman interaction, can select specific spin multiplicities. Silicon–vacancy defects have spin–quadruplet ground states which can be polarized through optical pumping. Continuous stimulated emission of microwaves from optically pumped silicon–vacancy defects in 6H–SiC has been reported recently<sup>7</sup>, but masing remained elusive.

In the 1960s, nitrogen impurities in diamond were proposed as potential maser gain media<sup>8–10</sup>, by using a four-spin-flip cross-relaxation mechanism to produce population inversion in paramagnetic spin-1/2 nitrogen donors. Charged nitrogen–vacancy (NV<sup>−</sup>) defect centres in diamond (Fig. 1a) were observed using electron paramagnetic resonance (EPR) almost 40 years ago<sup>11</sup>. The ability to prepare and read the quantum state of the triplet sublevels efficiently using optically detected magnetic resonance has enabled applications of NV<sup>−</sup> centres in magnetometry<sup>12–14</sup> and quantum information processing<sup>15</sup>. They were recently proposed as quantum emitters for room-temperature masers<sup>6</sup> owing to their attractive properties of long spin dephasing times (of greater than 1 μs), long spin-polarization lifetimes (of about 5 ms; refs 16, 17) and a triplet ground state that can be polarized through optical pumping<sup>6,18,19</sup>. Furthermore, diamond has the highest known thermal conductivity (10<sup>3</sup> W m<sup>−1</sup> K<sup>−1</sup>) and excellent mechanical properties, which obviates thermal runaway. Here we use ensembles of optically pumped NV<sup>−</sup> centres as the gain medium for a continuous-wave room-temperature maser oscillator.

The triplet ground state (<sup>3</sup>A<sub>2</sub>) of the NV<sup>−</sup> defect has a zero-field splitting *D* that places the quasi-degenerate |±1⟩ sublevels approximately 2.87 GHz above the |0⟩ sublevel (Fig. 1b)<sup>19</sup>. At room temperature and in zero magnetic field, the sublevels are populated according to Boltzmann statistics, with a few more electrons populating the lower |0⟩ sublevel than the higher |±1⟩ sublevels. The triplet ground state can be spin-polarized by pumping with optical radiation with wavelengths of around 532 nm (ref. 18), so that the |0⟩ sublevel becomes preferentially populated with respect to |±1⟩. On photo-excitation, electrons in the |0⟩ and |±1⟩ sublevels of the triplet ground state undergo spin-conserving transitions into an excited triplet state (<sup>3</sup>E). Spin-selective intersystem crossing preferentially transfers electrons from the |±1⟩ excited triplet-state sublevels to a metastable singlet state, which then decay non-radiatively back to the ground state, into the |0⟩ and |±1⟩ sublevels at roughly equal rates. In this manner, continuous optical pumping of the triplet ground state of the NV<sup>−</sup> defect can result in spin polarization whereby up to 80% of electrons reside in the |0⟩ sublevel<sup>19</sup>.

However, stimulated emission requires a positive population inversion. This can be achieved by applying a magnetic field along one of the four axes of the NV defects (Fig. 1a), which splits the energy of the |±1⟩ sublevels via the Zeeman interaction but leaves the |0⟩ sublevel unchanged (Fig. 1c). For an electron Zeeman interaction energy of  $\gamma_e \hbar B$ , greater than twice the zero-field-splitting energy  $\hbar D$  (for  $B \geq 102.5$  mT), the energy of the |−1⟩ sublevel dips below that of the |0⟩ sublevel, permitting a population inversion to be established. If the transition frequency  $\omega_s$  between the ground state |*g*⟩ ≡ |−1⟩ and the excited state |*e*⟩ ≡ |0⟩ is resonant with that of a cavity mode  $\omega_c$ , then

<sup>1</sup>Department of Materials, Imperial College London, Exhibition Road, London SW7 2AZ, UK. <sup>2</sup>London Centre for Nanotechnology, Imperial College London, Exhibition Road, London SW7 2AZ, UK.

<sup>3</sup>Institute of Structural and Molecular Biology, University College London, Gower Street, London WC1E 8BT, UK. <sup>4</sup>London Centre for Nanotechnology, 17–19 Gordon Street, London WC1H 0AH, UK.

<sup>5</sup>School of Biological and Chemical Sciences, Queen Mary University of London, Mile End Road, London E1 4NS, UK. <sup>6</sup>Department of Chemistry, University of Saarland, 66123 Saarbrücken, Germany.

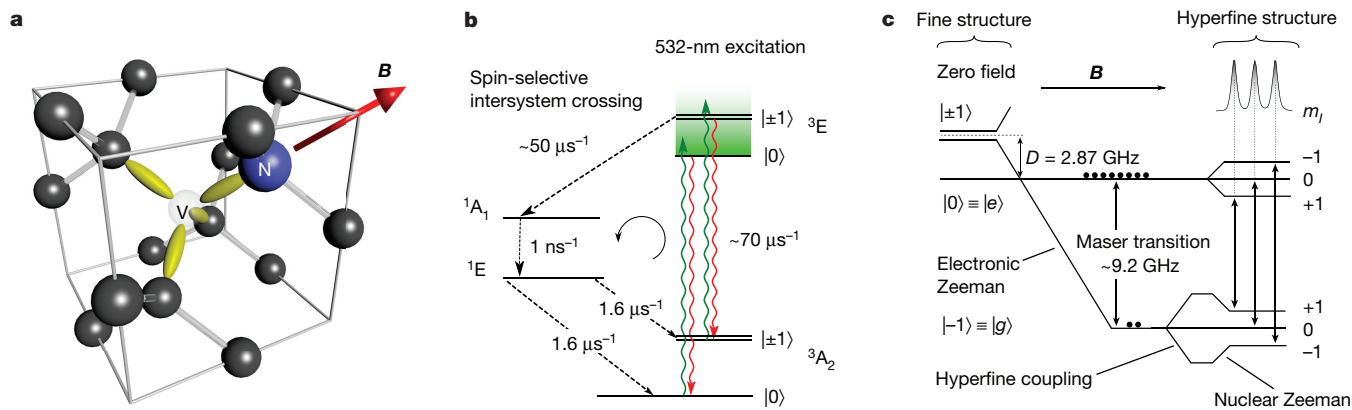


**Figure 1 | Structure of the NV<sup>-</sup> centres, optical pumping and magnetic-field interaction.** **a**, The NV<sup>-</sup> centre in diamond comprises a nitrogen atom (blue) adjacent to a vacancy (light grey), surrounded by carbon atoms (black). A magnetic field **B** (red arrow) is applied along the NV axis. **b**, The optical spin-polarizing pump process at zero-field. A continuous-wave 532-nm laser pumps electrons from the <sup>3</sup>A<sub>2</sub> triplet ground state into the triplet excited state <sup>3</sup>E via spin-conserving radiative transitions. Non-radiative spin-selective intersystem crossing transfers roughly 40% of the excited  $|\pm 1\rangle$  electrons into the singlet state <sup>1</sup>A<sub>1</sub> at a rate of 50 μs<sup>-1</sup>, which decay quickly (at a rate of 1 ns<sup>-1</sup>) into the metastable state <sup>1</sup>E, and then back to the triplet ground state with roughly equal probability of entering the  $|\pm 1\rangle$  or  $|0\rangle$  sublevels (at a rate 1.6 μs<sup>-1</sup>). The remaining electrons in the excited triplet state fluoresce back to the ground state

stimulated emission of microwave photons will occur. Furthermore, if the rate of stimulated emission of microwave photons exceeds the loss rate due to cavity dissipation, then build-up of the cavity-photon population occurs, resulting in maser oscillation.

For this study, we used a synthetic type-IIa diamond with a concentration of  $\text{NV}^-$  centres of 0.36 p.p.m. (Methods). The number of  $\text{NV}^-$  centres was estimated to be  $7.3 \times 10^{14}$ , of which roughly one in eighteen couple to the cavity mode, as a result of two of the three triplet sublevels being resonant on one of the four NV axes and one of the three  $^{14}\text{N}$  hyperfine lines, yielding  $N = 4.0 \times 10^{13}$  active  $\text{NV}^-$  centres. The longitudinal (spin-lattice) and transverse (spin-dephasing) relaxation times were measured at 9.5 GHz and room temperature (300 K) using EPR spectroscopy, yielding  $T_1 = 4.8$  ms and  $T_2^* = 0.5$   $\mu\text{s}$ , respectively (Methods). These values agree with those reported for samples with similar concentrations of nitrogen impurities<sup>16,17</sup>.

The cooperativity  $C = 4g_s^2 N / (\kappa_c \kappa_s)$  is a figure of merit for masers and lasers, where  $g_s$  is the single spin-photon coupling rate,  $\kappa_c = \omega_c / Q$  is the decay rate of the cavity mode,  $Q$  is the quality factor of the cavity and  $\kappa_s \approx 2/T_2^*$  the spin-dephasing rate. For above-threshold maser oscillation the cooperativity needs to be much greater than unity ( $C \gg 1$ ). The Purcell factor is key to enhancing maser performance<sup>2,20</sup> and contributes a factor of  $g_s^2 / \kappa_c$  to the cooperativity. A maser cavity with a high Purcell factor was designed and constructed using a hollow cylindrical single-crystal sapphire ring housed within a copper cavity. The cavity supports an axisymmetric transverse electric ( $TE_{01\delta}$ ) mode that resonates at 9.22 GHz with a loaded  $Q$  factor of 30,000. A magnetic mode volume of  $V_m = 0.15 \text{ cm}^3$  was calculated, yielding a single spin-photon coupling of  $g_s = 0.7 \text{ Hz}$  and an estimated ( $\sqrt{N}$ -enhanced) collective spin-photon coupling of  $g_e = 4.4 \text{ MHz}$  (Methods). This collective coupling, combined with the decay rate of the cavity mode  $\kappa_c \approx 1.9 \text{ MHz}$  and the measured spin-decoherence rate  $\kappa_s \approx 2/T_2^* = 3.9 \text{ MHz}$ , yields a cooperativity of  $C \approx 10.6$ , which indicates that the maser should oscillate above a threshold pump rate per active  $NV^-$  centre of  $w_{\text{thr}} \approx 300 \text{ s}^{-1}$ , equivalent to about 180 mW of optical power.

The cavity was positioned between the poles of an electromagnet (Bruker; Fig. 2) and oriented horizontally to allow optical access to continuous 532-nm laser excitation. The diamond was placed inside

by spin-conserving radiative processes at a rate of  $70 \mu\text{s}^{-1}$ . This process preferentially populates the  $|0\rangle$  sublevel, producing a spin-polarized triplet ground state<sup>6,18,19</sup>. c, The Zeeman and hyperfine interactions of NV centres. A magnetic field  $\mathbf{B}$  applied parallel to the NV<sup>-</sup> axis splits the  $|\pm 1\rangle$  states through the electronic and nuclear Zeeman interaction. For fields strengths of more than about 102.5 mT, the energy of the  $|-1\rangle$  state drops below that of the  $|0\rangle$  state, the difference at zero field being  $D \approx 2.87$  GHz. If the  $|0\rangle$  triplet sublevels are preferentially populated through optical pumping, then population inversion (with electrons depicted as black circles) is established. Hyperfine coupling between ( $S = 1$ ) spin triplets with adjacent  $^{14}\text{N}$  nuclear spins  $m_I$  (where  $I = 1$ ) produces three observable emission lines. The maser transition is between the  $|e\rangle \equiv |0\rangle$  and  $|g\rangle \equiv |-1\rangle$  states.

the sapphire ring and, using EPR spectroscopy, oriented so that one set of NV  $\langle 111 \rangle$  axes was aligned parallel to the magnetic field (Methods, Extended Data Fig. 1). EPR spectra were collected in the dark (Fig. 3a, b) and then laser excitation was applied with gradually increasing power. As the laser power increases, the high-field absorption lines decrease in amplitude until they disappear at a pump power of about 1.5 mW, owing to equalization of the  $|e\rangle$  and  $|g\rangle$  populations (zero spin

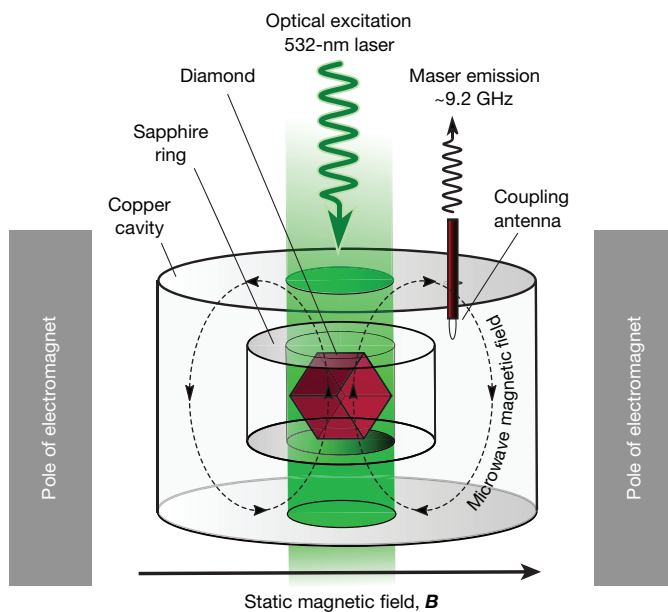


**Figure 2 | Diamond maser construction.** The diamond was placed inside the sapphire ring and, using EPR spectroscopy, oriented so that one set of NV(111) axes was aligned parallel to the magnetic field (Methods, Extended Data Fig. 1). The sapphire and diamond were housed within a cylindrical copper cavity, and a microwave loop antenna coupled the maser emission power into a transmission line. The diamond was optically pumped at 532 nm by a continuous-wave Nd:YAG laser.

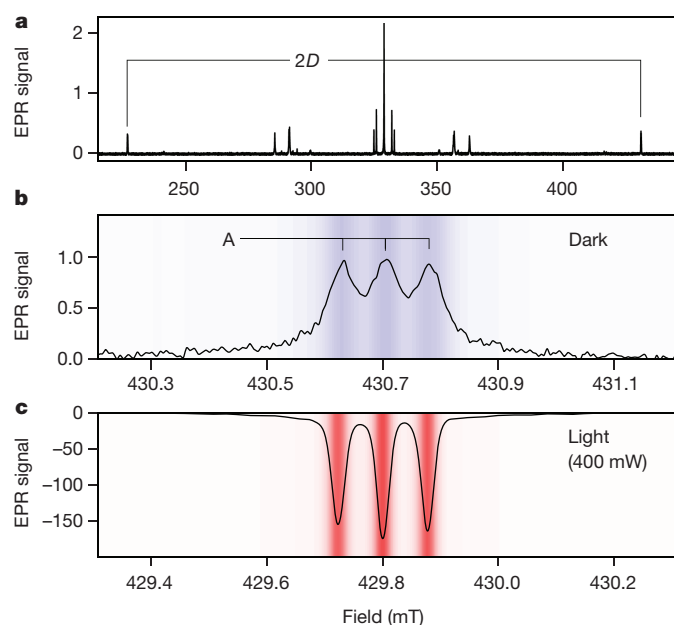


**Figure 3 | Electron paramagnetic resonance spectroscopy.** **a**, Wide EPR field sweep from 215 mT to 445 mT. The diamond sample was aligned to provide a maximum field splitting of  $2D \approx 102.5$  mT between the low-field and high-field lines. **b**, High-field absorption (blue shading) in the dark state, normalized to the maximum value. The three lines are separated by approximately  $A = 0.075$  mT, owing to the hyperfine coupling of ( $S = 1$ ) triplets with adjacent ( $I = 1$ )  $^{14}\text{N}$  nuclei. **c**, The lines become emissive (red shading) upon illumination by 400 mW of 532-nm laser light. The EPR signal amplitude is roughly 150 times greater than in the dark state and has shifted  $-25$  MHz in frequency (about 0.9 mT).

polarization). Modelling of the populations under optical pumping yields an equalization pump rate of  $w_{\text{eq}} = 1.5 \text{ s}^{-1}$ , corresponding to an estimated pump power of about 0.9 mW, which agrees well with the measured incident power. The low concentration of NV centres results in only 33% of the incident optical power being absorbed. Although this is far from optimal, it ensures that the NV centres are pumped almost homogeneously, because the laser intensity varies marginally across the sample.

When the laser pump power was increased to 400 mW (Fig. 3c), we observed a cavity frequency shift of  $-25$  MHz. We attribute this shift to an estimated  $35^\circ\text{C}$  increase in temperature of the sapphire ring and diamond, caused by heating. The observed EPR signal was a factor of about 150 greater in amplitude than for the dark state. Because the amplitude of the EPR signal is proportional to the difference in the populations of the  $|e\rangle$  and  $|g\rangle$  states (the spin polarization), it can be calibrated against the Boltzmann-populated dark state to provide an estimate of the population inversion,  $S^z = N_e - N_g \approx 0.09N$ , which agrees favourably with the predicted inversion<sup>6</sup>,  $S^z = \kappa_c \kappa_s / (4g_s^2) \approx 0.10N$ . Once the optical beam alignment and polarization were optimized for maximum emission on the high-field line and the cavity frequency had stabilized, the maser was disconnected from the EPR spectrometer and connected to a spectrum analyser (Advantest R3271A). The magnetic field was stepped across the high-field resonances using a programmable field controller (Bruker ER-032M) and the microwave output recorded at each magnetic field position. As depicted in Fig. 4a, three separate regions of continuous maser emission—corresponding to the three hyperfine transitions—were observed. The peak emission power of the maser was  $-90.3$  dBm (comparable with a hydrogen maser), with an estimated average pump rate per  $\text{NV}^-$  centre of  $w = 410 \text{ s}^{-1}$ . The maser emission persisted without degradation in power for the duration of all experiments (the longest being 10 h), demonstrating the robustness of the system. We repeated the experiment for different laser

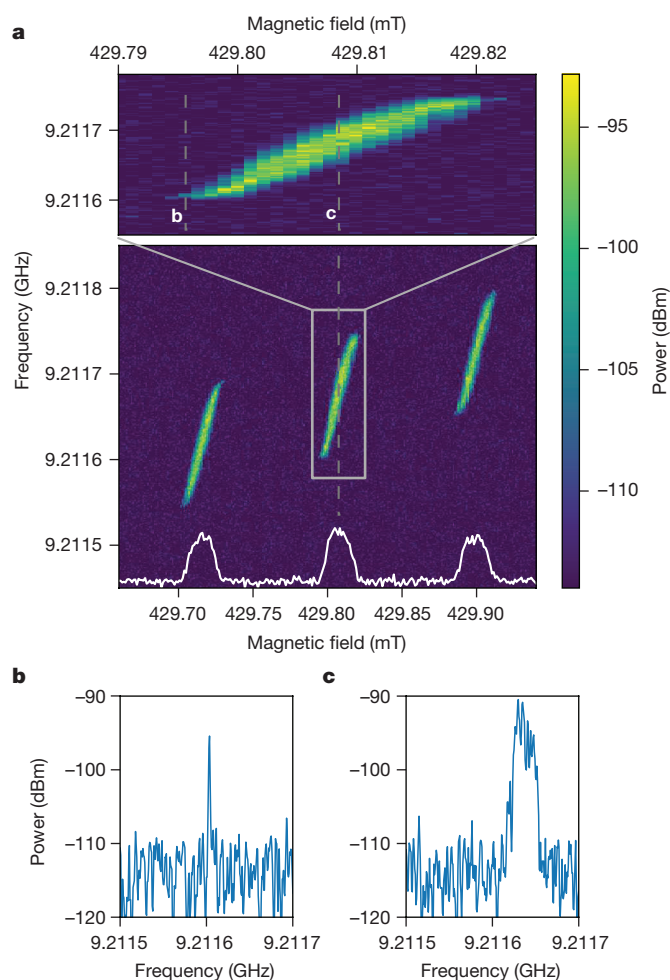


**Figure 4 | Field-frequency maser emission plots.** For an optical pump power of 400 mW, the static magnetic field  $B$  was varied from 429 mT to 431 mT in  $1\text{-}\mu\text{T}$  increments. At each field value, we recorded the spectral emission power that emerged from the maser. **a**, The maser emission spectral power (colour scale) as a function of applied magnetic field  $B$ . There are three regions of maser oscillation, which correspond to each of the hyperfine transitions. The white line shows the integrated power spectral density. The central region is magnified (top) to show the narrow-linewidth emission spectrum at the edge of the threshold (**b**) and the limit-cycle-broadened spectrum at the centre of the emission region (**c**). **b**, At the edge of the emission spectrum, slightly above threshold the emission has a narrow linewidth (about 50 Hz). **c**, At the centre of the emission region, the linewidth is broadened owing to the presence of limit cycles.

pump powers, which revealed threshold behaviour with a threshold pump power of 138 mW (Extended Data Fig. 2a).

At the edge of the maser emission region (Fig. 4b), the linewidth of approximately 50 Hz approaches the Schawlow–Townes limit<sup>21</sup> for the observed output power  $P_{\text{out}}$ ,  $\gamma_{\text{ST}} = \pi \hbar \omega_c \kappa_c^2 / (2P_{\text{out}}) \approx 10$  Hz. However, near the centre of the each emission region, the maser emission line appears broadened (Fig. 4c). Dynamical simulations of the photon population of the maser cavity reveal nonlinear oscillations that exhibit limit cycles<sup>22</sup> in the inversion–photon–population phase space. Further investigation revealed that these limit cycles are eliminated if the spin decay rate  $\kappa_c$  is increased (by increasing the concentration of NV centres) or if the spin–photon coupling rate  $g_s$  is decreased through detuning ( $\omega_c \neq \omega_s$ ), which explains their absence just above threshold (Fig. 4b).

We have achieved continuous maser operation by combining a cavity with a high Purcell factor with the narrow linewidth of the  $\text{NV}^-$  defect transitions in diamond. Although we used a frequency of 9.2 GHz in this study, which is close to the 9.193 GHz of a caesium



atomic clock, any frequency that is required may be produced by changing the magnetic field to be resonant at the appropriate frequency. We envisage that a diamond maser amplifier working at room temperature can find immediate application in deep-space communications and radio astronomy, where its ultralow noise would be beneficial in amplifying weak electromagnetic signals without the need for cryogenic cooling. Furthermore, ultrasensitive parametric detectors could be used in magnetic resonance, secure communications and high-precision metrology. Given that the fundamental process that occurs in a maser is the conversion of optical photons to coherent microwave photons<sup>20</sup>, we expect the field of diamond-based quantum optics to be an immediate beneficiary of this work, with the optical-microwave photon interface being key to the initialization, manipulation and detection of quantum states.

**Online Content** Methods, along with any additional Extended Data display items and Source Data, are available in the online version of the paper; references unique to these sections appear only in the online paper.

**Received 26 October 2017; accepted 19 January 2018.**

- Oxborrow, M., Breeze, J. & Alford, N. Room-temperature solid-state maser. *Nature* **488**, 353–356 (2012).
- Breeze, J. *et al.* Enhanced magnetic Purcell effect in room-temperature masers. *Nat. Commun.* **6**, 6215 (2015).
- Salvadori, E. *et al.* Nanosecond time-resolved characterization of a pentacene-based room-temperature maser. *Sci. Rep.* **7**, 41836 (2017).
- Poklonski, N., Lapchuk, N. & Lapchuk, T. Inverted EPR signal from nitrogen defects in a synthetic diamond single crystal at room temperature. *JETP Lett.* **80**, 748–751 (2004).
- Poklonski, N. *et al.* Nitrogen-doped chemical vapour deposited diamond: a new material for room-temperature solid state maser. *Chin. Phys. Lett.* **24**, 2088–2090 (2007).
- Jin, L. *et al.* Proposal for a room-temperature diamond maser. *Nat. Commun.* **6**, 8251 (2015).
- Kraus, H. *et al.* Room-temperature quantum microwave emitters based on spin defects in silicon carbide. *Nat. Phys.* **10**, 157–162 (2014).
- Smith, W., Sorokin, P., Gelles, I. & Lasher, G. Electron-spin resonance of nitrogen donors in diamond. *Phys. Rev.* **115**, 1546–1552 (1959).
- Sorokin, P., Lasher, G. & Gelles, I. Cross relaxation studies in diamond. *Phys. Rev.* **118**, 939–945 (1960).
- Siegman, A. *Microwave Solid-State Masers* Ch. 4 (McGraw-Hill, 1964).
- Loubser, J. & van Wyk, J. Electron spin resonance in the study of diamond. *Rep. Prog. Phys.* **41**, 1201–1248 (1978).
- Gruber, A. *et al.* Scanning confocal optical microscopy and magnetic resonance on single defect centers. *Science* **276**, 2012–2014 (1997).
- Taylor, J. *et al.* High-sensitivity diamond magnetometer with nanoscale resolution. *Nat. Phys.* **4**, 810–816 (2008); erratum **7**, 270 (2011).
- Maze, J. *et al.* Nanoscale magnetic sensing with an individual electronic spin in diamond. *Nature* **455**, 644–647 (2008).
- Childress, L. *et al.* Coherent dynamics of coupled electron and nuclear spin qubits in diamond. *Science* **314**, 281–285 (2006).
- Takahashi, S., Hanson, R., van Tol, J., Sherwin, M. S. & Awschalom, D. D. Quenching spin decoherence in diamond through spin bath polarization. *Phys. Rev. Lett.* **101**, 047601 (2008).
- Jarmola, A., Acosta, V., Jensen, K., Chemerisov, S. & Budker, D. Temperature- and magnetic-field-dependent longitudinal spin relaxation in nitrogen-vacancy ensembles in diamond. *Phys. Rev. Lett.* **108**, 197601 (2012).
- Robledo, L., Bernien, H., van der Sar, T. & Hanson, R. Spin dynamics in the optical cycle of single nitrogen-vacancy centres in diamond. *New J. Phys.* **13**, 025013 (2011).
- Doherty, M. W. *et al.* The nitrogen-vacancy colour centre in diamond. *Phys. Rep.* **528**, 1–45 (2013).
- Breeze, J. D. *et al.* Room-temperature cavity quantum electrodynamics with strongly coupled Dicke states. *npj Quantum Inf.* **3**, 1 (2017).
- Schawlow, A. L. & Townes, C. H. Infrared and optical masers. *Phys. Rev.* **112**, 1940–1949 (1958).
- Dimer, F., Estienne, B., Parkins, A. & Carmichael, H. Proposed realization of the Dicke-model quantum phase transition in an optical cavity QED system. *Phys. Rev. A* **75**, 013804 (2007).

**Acknowledgements** We thank J. Hall and M. Markham (Element 6 Ltd) for supplying the diamond samples, P. French and R. Taylor (Photonics Group at Imperial College London) for lending us their continuous-wave laser, and E. Bauch (Harvard University) for discussions. We also thank M. Lennon (IC), D. Halpin and D. Farquharson (UCL) for manufacturing the cavity components. This work was supported by the UK Engineering and Physical Sciences Research Council through grants EP/K011987/1 (IC) and EP/K011804/1 (UCL). We also acknowledge support from the Henry Royce Institute.

**Author Contributions** J.D.B. conceived the study, developed the theory, designed the maser cavity, devised the experiment and wrote software for collecting experimental data. J.D.B. and C.W.M.K. developed the experimental design and performed experiments with input from E.S. and J.S. J.D.B. interpreted the results with input from E.S. and C.W.M.K. J.S. characterized the diamond NV concentration by optical means and developed the optical pumping scheme. J.D.B., E.S. and C.W.M.K. characterized the diamonds using EPR. J.D.B. wrote the paper with assistance from C.W.M.K. and with additional editing by E.S. and N.M.A.

**Author Information** Reprints and permissions information is available at [www.nature.com/reprints](http://www.nature.com/reprints). The authors declare no competing financial interests. Readers are welcome to comment on the online version of the paper. Publisher's note: Springer Nature remains neutral with regard to jurisdictional claims in published maps and institutional affiliations. Correspondence and requests for materials should be addressed to J.D.B. ([jonathan.breeze@imperial.ac.uk](mailto:jonathan.breeze@imperial.ac.uk)).

**Reviewer Information** *Nature* thanks A. Blank, F. Jelezko and R.-B. Liu for their contribution to the peer review of this work.

## METHODS

**Spin Hamiltonian.** The spin Hamiltonian for NV<sup>−</sup> centres in diamond is given by<sup>23</sup>

$$H_{\text{spin}} = \gamma_e \mathbf{S} \cdot \mathbf{B} - \gamma_n \mathbf{I} \cdot \mathbf{B} + D \left[ S_z^2 - \frac{1}{3} S(S+1) \right] + SA\mathbf{I}$$

where  $\gamma_e$  and  $\gamma_n$  are the gyromagnetic ratios of electrons and nuclei, respectively,  $D \approx 2.87$  GHz is the fine structure zero-field splitting,  $\mathbf{S}$  and  $\mathbf{I}$  are the triplet spin and <sup>14</sup>N nuclear spin eigenvectors, respectively,  $A$  is the uniaxially anisotropic hyperfine coupling tensor ( $A_{\perp} = -2.7$  MHz,  $A_{\parallel} = -2.1$  MHz with respect to the NV axis) and  $\mathbf{B}$  is the magnetic field.

**Spin-photon maser dynamics.** The maser is modelled as an ensemble of  $N$  two-level quantum emitters (lower state  $|g\rangle \equiv |-1\rangle$  and upper state  $|e\rangle \equiv |0\rangle$ ) resonantly coupled to a cavity mode. The distance between the emitters is much less than the wavelength of the cavity mode and their spin-photon coupling is assumed to be homogeneous. This interaction can be described by the Tavis–Cummings Hamiltonian<sup>24</sup> within the rotating-wave approximation:

$$H_{\text{TC}} = \hbar\omega_c a^\dagger a + \frac{1}{2} \hbar\omega_s S^z + \hbar g_e (S^+ a + a^\dagger S^-)$$

where  $g_e = g_s \sqrt{N}$  is the enhanced collective spin–photon coupling strength,  $g_s$  is the single spin–photon coupling strength,  $\omega_c$  is the cavity frequency,  $\omega_s$  is the (two-level) transition frequency of the spin,  $a^\dagger$  ( $a$ ) is the creation (annihilation) operator of the cavity photon,  $S^z$  is the collective inversion operator,  $S^\pm$  are the normalized collective spin operators and  $\hbar$  is the reduced Planck constant. The single spin–photon coupling can be written as<sup>25</sup>

$$g_s = \gamma_e \sqrt{\frac{\mu_0 \hbar \omega_c \kappa_s / (\kappa_s + \kappa_c)}{2V_m (1 + \Delta^2)}}$$

where  $\Delta = 2(\omega_c - \omega_s)/(\kappa_s + \kappa_c)$  is a spin–cavity detuning parameter. The Hamiltonian, coupled with a dissipative Liouvillian, permits Lindblad master equations to be developed for the expectation values of the cavity field operator  $a$ , inversion  $S^z$  and transverse spin  $S^\pm$  operators. These can be solved in the steady state, leading to a simple maser threshold pumping rate per NV centre of

$$w_{\text{thr}} = \gamma(C - 1)^{-1}\eta$$

where  $C = 4g_s^2 N / (\kappa_s \kappa_c)$  is the cooperativity,  $\gamma = 1/T_1$  is the spin–lattice relaxation rate and  $\eta$  is a scaling factor based on the number of photons required to increase the inversion by one. The scaling factor  $\eta$  can be derived from the steady-state optical pump rate equations. We derived a value of  $\eta \approx 14.4$ ; it holds for pump rates up to  $w_{\text{thr}}$  at which the populations of the  $|\pm 1\rangle$  states are approximately equal. This is the maser amplification regime in which the inversion, given by  $S^z = wN/(w + \eta\gamma)$ , is positive. Accessing this regime is not challenging because the dark-state populations of the triplet ground states have approximately equal Boltzmann populations, which require only weak optical pumping for the inversion to become positive. One noticeable aspect of the threshold equation is that  $w_{\text{thr}}$  is lower than the scaled spin–lattice relaxation rate  $\eta\gamma$  if  $C > 1$ , which can be considered the condition for masing. The inversion in the maser oscillation regime

$$S^z = N_e - N_g = \kappa_s \kappa_c / (4g_s^2) = N/C$$

is always less than  $N$  when  $C > 1$ . Above threshold and for steady-state conditions, we solve a nonlinear system of rate equations comprising seven NV<sup>−</sup> states (triplet ground, triplet excited and singlet), a cavity field operator  $\hat{a}$ , a longitudinal (inversion) operator  $\hat{S}^z$  and a transverse spin operator  $\hat{S}^\pm$ . These equations are the Maxwell–Bloch equations coupled to a set of optical spin dynamical rate equations. **Diamond preparation and characterization.** A synthetic diamond with natural carbon isotopic abundance, doped with approximately 5 p.p.m. of nitrogen donors was grown by chemical vapour deposition. The diamond was irradiated by 4.5-MeV electrons, equivalent to a dose of  $5 \times 10^{18} \text{ cm}^{-2}$ , to create vacancies. It was then annealed for 2 h at 400 °C, 16 h at 800 °C and a further 2 h at 1,200 °C to promote the formation of NV defect centres. The diamond was laser-cut into a cuboid of dimensions 2.1 mm  $\times$  2.1 mm  $\times$  2.6 mm, with {100} faces and {111} crystal directions (along which the NV centres lie) emerging from the corners of the cuboid. These steps were performed by Element 6 (UK). The diamond was cleaned in nitric acid to remove residual graphitic carbon (48 h) and then polished using a lint-free cloth.

NV defect centres exist in neutral NV<sup>0</sup> and charged NV<sup>−</sup> states. Using ultraviolet–visible absorbance spectroscopy (Cary 5000 UV–VIS–NIR spectrophotometer, Ocean Optics USB 2000+ fibre optic spectrometer), the NV<sup>−</sup> concentration in the

sample was found to be 0.36 p.p.m. Further photoluminescence studies revealed that the ratio of charged to neutral NV centres (NV<sup>−</sup>/NV<sup>0</sup>) was approximately 0.55 under illumination from a 100-mW continuous-wave 532-nm Nd:YAG laser. Furthermore, the ratio decreased slightly as the laser power was reduced, suggesting that some NV<sup>−</sup> states had been photo-converted into NV<sup>0</sup> ones<sup>26,27</sup>. The total concentration of NV<sup>0</sup> and NV<sup>−</sup> states was  $[NV] \approx 1$  p.p.m., which, given the initial nitrogen concentration of  $[N^0] \approx 5$  p.p.m., equates to a N-to-NV conversion efficiency of 20%. The final nitrogen (P1 centre) concentration would be  $[N^0] \approx 4$  p.p.m. in this case.

**EPR spectroscopy of NV centres.** EPR spectroscopy at 9.5 GHz was used to align the diamond sample and measure the relaxation times  $T_1$ ,  $T_2$  (Bruker Elexsys E580 spectrometer with ER 4118 X-MD5 resonator) and  $T_2^*$  (Bruker EMXplus with ER 4122SHQ resonator) of the high-field line. The diamond was held inside a hollow low-loss quartz tube and oriented inside the cylindrical single-crystal sapphire ring of the resonator so that two NV axes lay in a plane perpendicular to the cylindrical axis. The diamond was rotated about the cylindrical axis of the cavity until the magnetic field was aligned with one of the two  $\langle 111 \rangle$  directions and colinear with a NV-defect axis. This was achieved by sweeping the magnetic field from 200 mT to 450 mT and noting the minimum and maximum fields at which absorption and emission occurred. When the difference in magnetic field between the low-field and high-field lines was equal to twice the zero-field splitting  $4\pi D/\gamma_e$  or 205 mT, the absorption peaks associated with the other three  $\langle 111 \rangle$  directions coalesced, becoming quasi-degenerate at about 370 mT. Pronounced low-field absorption and high-field emission peaks appeared at 239 mT and 444 mT, respectively. Nitrogen spin-1/2 (P1) impurities were evident at 341 mT. The spin–lattice relaxation time ( $T_1$ ) was measured using an inversion recovery sequence  $\pi$ – $T$ – $\pi/2$ – $\tau$ – $\pi$ – $\tau$ –echo, in which the interpulse delay  $\tau$  was kept fixed at 1.2  $\mu$ s and the time interval  $T$  was incremented in steps of 10  $\mu$ s from an initial value of 1  $\mu$ s. The length of the  $\pi/2$  pulse was 200 ns and each dataset comprised 1,024 points. The magnetic field was set on resonance with the  $m_I = 0$  hyperfine line of the highest EPR band (Fig. 1c). The homogeneous spin relaxation time ( $T_2$ ) was measured using a Hahn-echo sequence  $\pi/2$ – $\tau$ – $\pi$ – $\tau$ –echo, in which the interpulse delay  $\tau$  was incremented in steps of 80 ns from an initial value of 1.2  $\mu$ s. These measurements were repeated for increasing levels of optical pump power (Extended Data Fig. 2b, c). The inhomogeneous spin dephasing time  $T_2^*$  was measured using the saturation broadening technique (Extended Data Fig. 2d). The  $m_I = 0$  linewidth was measured as a function of applied microwave power. By extrapolating a linear fit of linewidth-squared versus microwave power down to zero power, the inhomogeneous broadening and hence  $T_2^*$  can be found.

**Maser cavity.** A high-Purcell-factor cavity was designed using a radial mode-matching technique<sup>28</sup>. The cavity comprised a single-crystal sapphire dielectric ring resonator (relative electrical permittivity  $\epsilon_r = 9.394$ ; outer diameter, 10 mm; inner diameter, 5.1 mm; height, 6.0 mm) housed centrally within an oxygen-free high-conductivity copper cavity (diameter, 36 mm; height, 28 mm). The cavity supported a TE<sub>018</sub> mode resonating at 9.22 GHz with an unloaded  $Q$  factor of 55,000. The central bore containing the diamond had an electric filling factor of 0.008, allowing the dielectric properties of the diamond to be neglected. A magnetic mode volume of  $V_m = 0.15 \text{ cm}^3$  was calculated from the ratio of the stored magnetic energy within the cavity to the maximum magnetic field energy density:

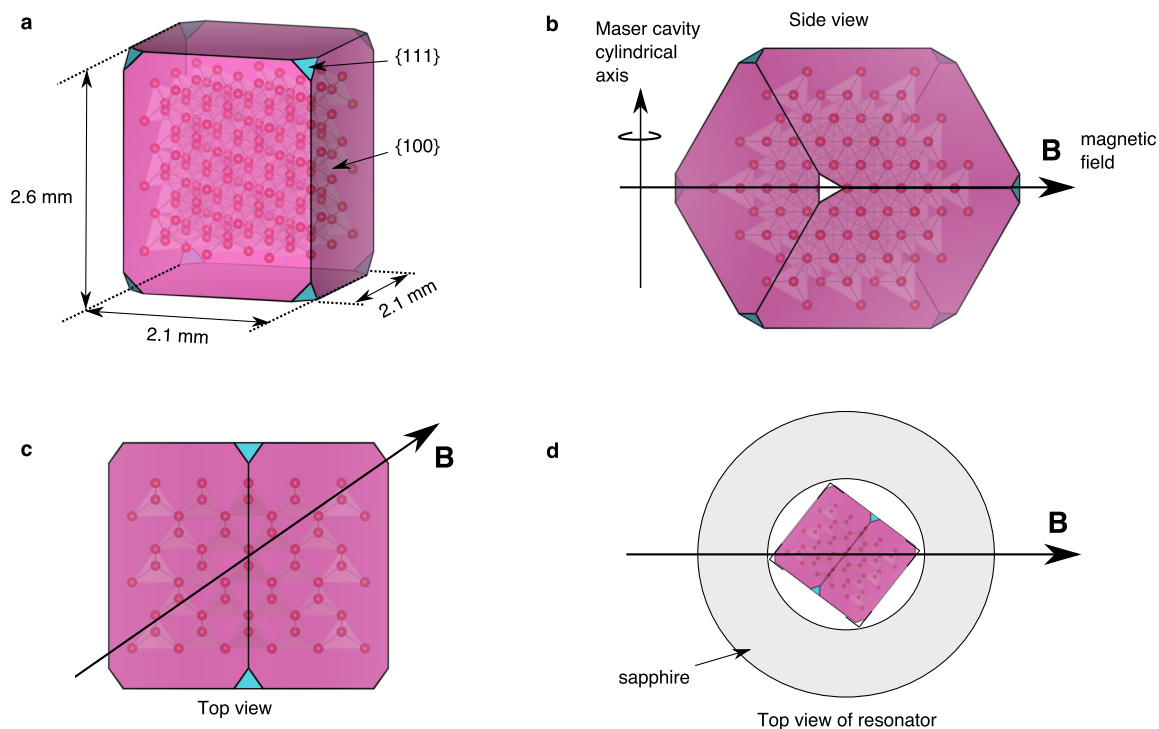
$$V_m = \int \frac{|\mathbf{H}(\mathbf{r})|^2}{|\mathbf{H}_{\text{max}}(\mathbf{r})|^2} dV$$

The electric filling factor of the sapphire was 0.76 and the magnetic filling factor of the central hole was 0.14. The diamond was mounted inside the sapphire resonator and held in place by quartz tubes. Coupling to the cavity was achieved by a small adjustable antenna loop, set slightly below critical coupling ( $k = 0.85$ ) to yield a loaded  $Q$  factor of 30,000.

**Optical pumping.** A continuous-wave 532-nm laser was used to pump the NV<sup>−</sup> centres (Laser Quantum Finesse Pure) with a spot size of 2.5 mm. The laser beam was adjusted until it was colinear with the cavity axis and  $p$ -polarized with respect to the surface of the diamond, because the angle of incidence was close to the Brewster angle (67.2°). The one-photon absorption cross-section of NV<sup>−</sup> centres at 532 nm is  $\sigma = 3.1 \times 10^{-17} \text{ cm}^2$  (ref. 29). The power required to pump the NV centres at rate  $w$  is therefore  $P_p \approx \hbar w \omega_p (A/\sigma)$ , where  $\omega_p$  is the pump frequency and  $A$  is the area (spot size). The defect pump rate  $w = \sigma I / (\hbar \omega_p)$ , where  $\omega_p$  the optical pump frequency, is proportional to the local pump intensity  $I = P_p/A$ , which varies across the sample.

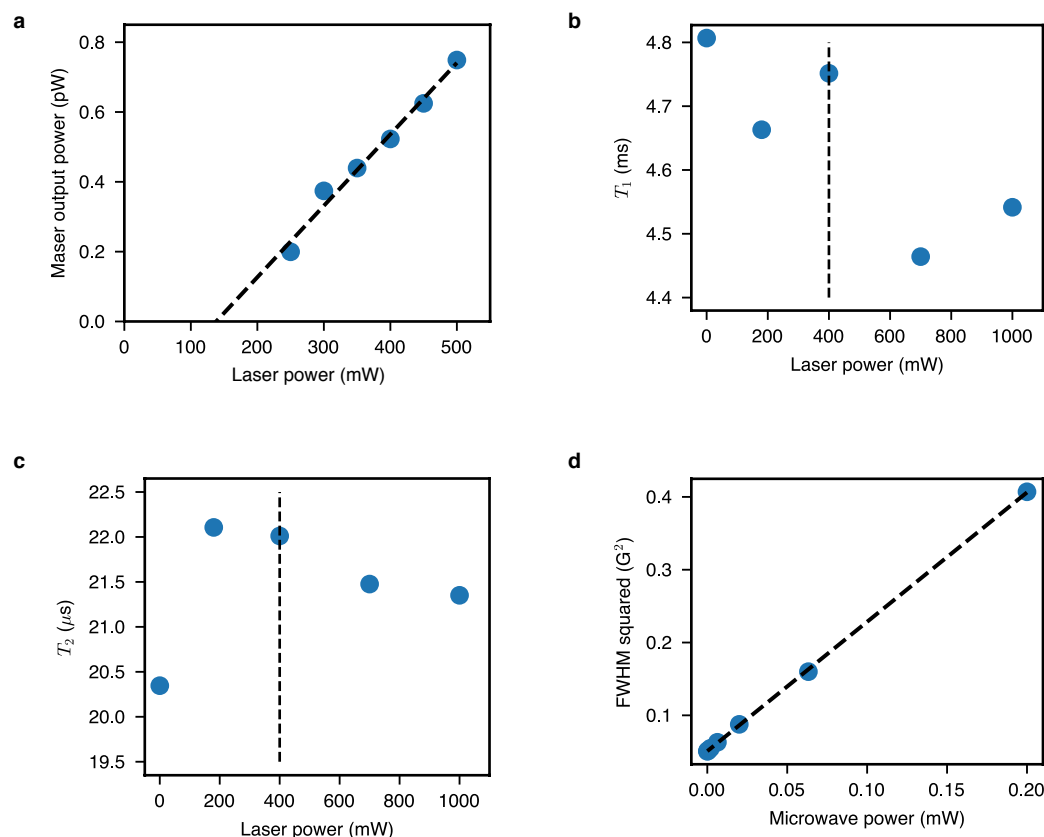
**Data availability.** The data that support the findings of this study are available from the corresponding author on reasonable request.

23. Yavkin, B., Mamin, G. & Orlinskii, S. High-frequency pulsed endor spectroscopy of the NV<sup>-</sup> centre in the commercial HPHT diamond. *J. Magn. Reson.* **262**, 15–19 (2016).
24. Tavis, M. & Cummings, F. W. Exact solution for an *N*-molecule radiation-field Hamiltonian. *Phys. Rev.* **170**, 379–384 (1968).
25. Carmichael, H. J. *Statistical Methods in Quantum Optics 1: Master Equations and Fokker-Planck Equations* Ch. 7 (Springer, 2003).
26. Manson, N. & Harrison, J. Photo-ionization of the nitrogen-vacancy center in diamond. *Diamond Related Materials* **14**, 1705–1710 (2005).
27. Aslam, N., Waldherr, G., Neumann, P., Jelezko, F. & Wrachtrup, J. Photo-induced ionization dynamics of the nitrogen vacancy defect in diamond investigated by single-shot charge state detection. *New J. Phys.* **15**, 013064 (2013).
28. Kajfez, D. & Guillon, P. *Dielectric Resonators* 1st edn, Ch. 5 (Artech House, 1964).
29. Wee, T.-L. *et al.* Two-photon excited fluorescence of nitrogen-vacancy centers in proton-irradiated type Ib diamond. *J. Phys. Chem. A* **111**, 9379–9386 (2007).



**Extended Data Figure 1 | Diamond sample geometry and orientation.** **a**, The diamond is a rectangular cuboid with dimensions  $2.1 \text{ mm} \times 2.1 \text{ mm} \times 2.6 \text{ mm}$ . The main faces (pink) are  $\{100\}$ , with the  $\{111\}$  faces (to which the NV  $\langle 111 \rangle$  directions are normal) depicted in blue. **b**, Side view of the diamond oriented within the maser cavity, with static magnetic field  $B$  applied across the NV  $\langle 111 \rangle$  direction. The microwave

magnetic field is perpendicular to the N–V defect axis and static magnetic field direction. **c**, Top view of the diamond when it is oriented inside the cavity. **d**, Top view of the diamond placed within the single-crystal sapphire ring within the maser cavity. The depiction of the structure of diamond within the crystals (carbon atoms, bonds and tetrahedral) are for illustrative purposes only.



### Extended Data Figure 2 | Threshold and spin-relaxation measurements.

**a**, Maser threshold. The peak maser output power increases linearly as a function of the optical pump power (data). Extrapolation of the linear fit (dashed line) to zero maser output power reveals a threshold optical pump power of 138 mW, which is lower than the predicted 180 mW. **b**, Spin-lattice relaxation time  $T_1$  as a function of laser pump power (data). The slight decrease in  $T_1$  is expected and due to an increase in temperature caused by the non-radiative (heating) processes during the NV spin-polarizing optical pump cycle. **c**, Spin-decoherence time  $T_2$  as a function of laser pump power (data). There is little change in  $T_2$ , with a slight jump upon applying optical pumping, probably due to an increase in EPR signal

amplitude and hence less error. There is subsequently a slight decrease due to temperature increase and pumping decoherence. Photo-conversion of  $NV^-$  to  $NV^0$  could also be a source of decoherence. **d**, Power saturation broadening. The inhomogeneous spin decoherence time  $T_2^* = 2/\kappa_s$  was inferred from power saturation broadening measurements of the spin resonance lines. The spectral full-width at half-maximum (FWHM)  $\gamma$  was measured as a function of interrogating microwave power (data). A spin decoherence rate of  $T_2^* = 0.52 \mu s$  was extracted by extrapolating the square of the FWHM linewidth down to zero microwave power (dashed line). The vertical dashed line in **b** and **c** depicts the applied optical pump power of 400 mW.